

Dong Sung Kim · Tai Hun Kwon

Modeling, analysis and design of centrifugal force-driven transient filling flow into a circular microchannel

Received: 18 November 2004 / Accepted: 9 March 2005 / Published online: 15 September 2005
© Springer-Verlag 2005

Abstract Recently, centrifugal pumping has been regarded as an excellent alternative control method for fluid flow inside microchannels. In this paper, we have first developed the physical modeling and carried out the analysis for the centrifugal force-driven transient filling flow into a circular microchannel. Two types of analytic solutions for the transient flow were obtained: (1) pseudostatic approximate solution and (2) exact solution. Analytic solutions include expressions for flow front advancement, detailed velocity profile and pressure distribution. The obtained analytic results show that the filling flow driven by centrifugal force is affected by two dimensionless parameters which combine fluid properties, channel geometry and processing condition of rotational speed. Effects of inertia, viscous and centrifugal forces were also discussed based on the parametric study. Furthermore, we have also successfully provided a simple and convenient analytic design tool for such microchannels, demonstrating two design application examples.

Keywords Transient filling flow · Centrifugal force · Microchannel · Modeling · Analysis

1 Introduction

Over the past decade, wide applications of integrated microfluidic systems have been found in the fields of

miniaturized analytic systems for chemistry and biology such as genomic and proteomic analyses, clinical diagnostics and micro total analysis systems (Manz et al. 1990; Sanders and Manz 2000; Reyes et al. 2002; Auroux et al. 2002). In recent years, these miniaturized analytic microfluidic systems enable a point-of-care or ubiquitous diagnosis and treatment of patients with minimizing sample and reagents volumes.

The integrated microfluidic systems generally contain several microfluidic functions (Reyes et al. 2002; Auroux et al. 2002; Kovacs 1998) such as pump, valve, mixing, reaction, separation and so on. In order to achieve desirable functions with the microfluidic systems in a precise manner, the control of the fluid flow is inherently required. Amongst many controlling methods reported in the literature, electrokinetic and pressure-driven flow controls have been regarded as the most representative control methods. Electroosmotic flow has widely been utilized for the analyses in which a separation process is involved in microfabricated capillaries due to its interesting characteristic of a plug-like velocity profile (Effenhauser et al. 1997; Probst 1994). Numerous experimental and analytic studies were carried out to understand flow characteristics of the electrokinetic flow for the purpose of the proper design and improvement of such microfluidic systems (Herr et al. 2000; Ross et al. 2001; Xuan and Li 2004). Electrokinetic control, however, has the following disadvantages: (1) high sensitivity to physicochemical properties of fluids and substrates; (2) requirement of a high-voltage power supplier; (3) possible working limitation due to the bubble existence or formation inside a channel; (4) difficulty in achieving high flow rate ($\leq 1 \mu\text{L s}^{-1}$) (Probst 1994; Duffy et al. 1999). In contrast, when there is no separation process involved, the pressure-driven flow control is quite manageable with respect to the flow rate and the physicochemical properties of fluids and substrates. The pressure-driven laminar flow has been well understood and characterized in the macroscale duct. However, it was found that there is a little difference between the microscale laminar flow and the macroscale one. In this

D. S. Kim · T. H. Kwon (✉)
Department of Mechanical Engineering,
Pohang University of Science and Technology (POSTECH),
San 31 Hyoja-dong Nam-gu, Pohang,
Kyungbuk 790-784, Korea
E-mail: thkwon@postech.edu
Tel.: +82-54-2792175
Fax: +82-54-2795899

D. S. Kim · T. H. Kwon
Research Center for Micro Mechanical Systems,
Pohang University of Science and Technology (POSTECH),
San 31 Hyoja-dong Nam-gu, Pohang,
Kyungbuk 790-784, Korea

regard, many experimental and analytic studies of the pressure-driven flow in the microchannel were also performed in order to understand the microscale flow behavior (Koo and Kleinstreuer 2003). In addition to the studies of the steady-state flow in the microchannel, a transient filling flow into the microchannel was also studied experimentally and numerically (Kim et al. 2002; Tseng et al. 2002).

Recently, a centrifugal pumping method for a CD-type microfluidic chip equipped with a rotational motor was reported as a new controlling method of flow in microchannels (Duffy et al. 1999; Madou et al. 2001; Gyros Microlaboratory). The centrifugal force generates fluid flow with a little sensitivity to the physicochemical properties of the working fluid such as ionic strength, pH and so on (Duffy et al. 1999). It can also provide parallel pumping flows to several microchannels simultaneously on the same CD-type microfluidic chip. It is important to understand the spatial and temporal behavior of the fluid flow inside the microchannel for a precise design of a centrifugal microfluidic channel system. So far, most of previous studies in the literature simply adopted capillary stop valves making use of a surface tension effect for the purpose of controlling fluid flow, with lack of detailed understanding of the centrifugal flow behavior.

Numerical simulation could help us to design the desirable microchannel system more precisely and to understand the physical behavior of such microchannel flows. However, relying on a numerical analysis tool is very time consuming and costly at the first design step, especially for the cases of a complex microchannel network system or transient filling flow into microchannels. In contrast, an analytic solution approach, if available, provides a physical insight into fluid flow behavior inside the microfluidic channel. And moreover, it can also offer a simple design guide at the first design step so that the design time and cost could be remarkably reduced. But, to the best of our knowledge, there has been no report in the literature with regard to an analytic approach to the transient flow into the microchannel in which the fluid is driven by the centrifugal force.

In this paper, we first define a specific physical problem for the radial flow into a microchannel on a rotating disk, as a simplified model of the centrifugal flow. For such a model problem, a physical modeling is carried out based on the fundamental balance equations of mass and force. A dimensional analysis is then performed to understand the effects of related forces to the defined system according to the physical modeling. Two analytic solutions are obtained: (1) a pseudostatic approximation when the inertia force is negligible and (2) an exact solution with taking into account the inertia force. The solution provides an important information such as filling flow front advancement, velocity profile and pressure distribution as functions of both time and geometry. The obtained analytic results show that the filling flow driven by centrifugal force is affected by two dimensionless parameters, which combine fluid proper-

ties, channel geometry and rotating conditions. Finally, we propose a design tool for a microchannel in which the flow is driven by centrifugal force with application examples.

2 Problem statement

This paper aims not only at analyzing the transient filling flow into the microchannel, which is driven by a centrifugal pumping but also at providing a simple design tool to determine microchannel geometry and disk rotational speed to meet a specific flow requirement for the given fluid material properties. The analytic results will enable us to gain the physical insight to this centrifugal channel flow.

In this regard, we define a model problem to represent the transient flow into a microchannel driven by the rotation of a disk in this section. At this time, we focus on the circular cross-sectional microchannel as the first solution attempt. The model problem might be stated as follows.

Figure 1 shows a schematic diagram of a circular cross-sectional microchannel on a CD-type centrifugal microfluidic system. The hydraulic radius of the channel is denoted by R_h . A sample fluid, such as reagents or drugs having physical fluid properties of density, ρ and viscosity, μ , is injected into a reservoir, which is placed at a certain radial location of the CD plate such that the microchannel starts from the radial location of L_0 away from the center of the CD plate as shown in Fig. 1. Now consider the fluid flow when a rotational motor starts rotating the CD plate in a constant rota-

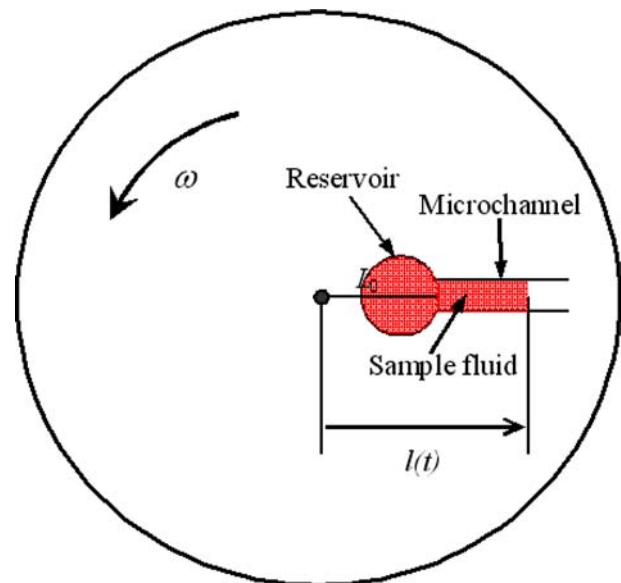


Fig. 1 Schematic diagram of the transient filling flow into a circular microchannel on the CD-type centrifugal microfluidic system. *Dark red area* represents a region occupied by the sample fluid, $l(t)$ indicating the flow front

tional speed of ω . The material will flow from the reservoir into the microchannel due to the centrifugal force and the flow front gradually advances along the radial direction of the CD plate. It is of our interest to be able to determine the flow front advancement as a function of time t , denoted by $l(t)$. Of course, this flow front advancement will depend on the rotational speed ω as well as the location of reservoir, channel geometry and material properties.

As for the design aspect of a microfluidic system with several microchannels on a CD plate, suppose a design objective is to deliver sample fluids to specific *desired locations* in the disk at *desired times* through the multiple microchannels via centrifugal force induced by the rotational motion of the CD plate. A designer has to decide where to put the reservoirs (L_0), and the hydraulic radii (R_h) for each channels along with the rotational speed (ω) of the disk. With this kind of design objective in mind, a simple analytic solution is indeed for a great use in designing such a microfluidic system utilizing the centrifugal mechanism. For instance, if the analytic expression of $l(t)$ is available in terms of the design parameters, i.e., fluid properties, microchannel geometry and processing conditions, one can easily design the centrifugal microchannel system.

In this regard, we would like to obtain an analytic solution for $l(t)$ as a function of time for a given sample fluid (ρ and μ), microchannel geometry (R_h and L_0) and processing condition (ω), which are regarded as the important design parameters in the centrifugal microchannel system. Of course, in obtaining an analytic solution for $l(t)$, we also find expressions of the detailed velocity profile as well as the pressure distribution for the transient filling flow inside the microchannel. Finally, we suggest a simple analytic design tool of a microchannel on the CD plate for the given conditions.

3 Physical modeling and governing equations

Figure 2 shows various forces applied to an infinitesimal control volume of fluid inside the centrifugal microchannel of a circular cross-section. The centrifugal force is developed in the downchannel direction, i.e., the radial direction of the CD plate. Shear force and pressure are also developed according to the fluid flow. To investigate the centrifugal force-driven transient flow analytically, we simplified the complicated problem by introducing

several assumptions described below and then derived governing equations associated with the transient flow.

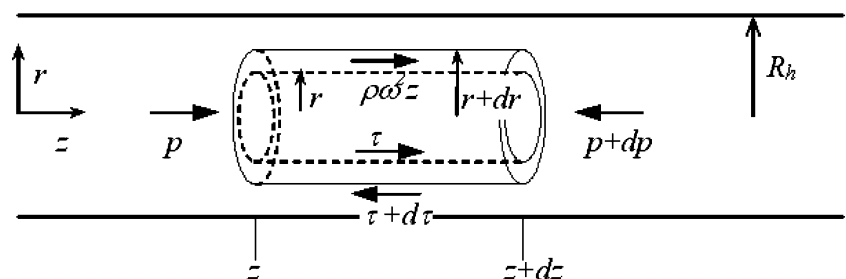
3.1 Assumptions

Assumption 1 In this study, as a simple constitutive equation, material is assumed to be a Newtonian fluid. (Non-Newtonian case needs a numerical simulation method since there is no analytic solution available.)

Assumption 2 As the first attempt to obtain analytic solutions for the transient flow into a microchannel, the Coriolis force effect is assumed to be negligible in a mild rotational speed in comparison with the centrifugal force effect. (Brenner et al. (2003) showed that the Coriolis force dominantly affects the flow over the rotational speed of 350 rad s^{-1} , or equivalently about 3,350 rpm, for a microchannel of which width and depth are 360 and $125 \mu\text{m}$, respectively. The Coriolis force induces the transversal flow inside the microchannel relative to the axial downchannel flow so that the flow becomes fully three dimensional. At the relatively low rotational speed, however, the Coriolis force could be neglected relative to the centrifugal force.) Under this assumption, the flow can be assumed to be an axial flow, i.e., $u_r = u_\theta = 0$ and $u_z \neq 0$ where u_r , u_θ and u_z are velocity components in the direction of r , θ and z , respectively, in a cylindrical coordinate system.

Assumption 3 Surface tension effect is neglected in this study, again as the first attempt to obtain analytic solutions for the transient flow into a microchannel. (It might be noted here that surface tension becomes an important parameter for the microscale transient flow (Duffy et al. 1999; Kim et al. 2002; Tseung et al. 2002; Madou et al. 2001; Gyros Microlaboratory) depending upon the surface properties. However, it may be reasonable to neglect the surface tension effect when a polymer substrate of which the contact angle of a sample fluid is almost 90° . For example, the contact angles between water and native surfaces of PDMS (polydimethylsiloxane) and COC (cyclic olefin copolymer) substrates are about 90° (Duffy et al. 1999) and 92° (Puntambekar 2002), respectively, with no surface modification. With this kind of case in mind, we ignored the surface tension effect for a simplified model problem.)

Fig. 2 An infinitesimal control volume of fluid with the applied forces inside circular microchannel in which flow is driven by centrifugal force



3.2 Governing equations

The local continuity equation for an axial downchannel flow assumption ($u_r = u_\theta = 0$) is simply,

$$\frac{\partial u_z}{\partial z} = 0, \quad (1)$$

which implies that the symmetric velocity profile of u_z is independent of z , i.e., $u_z = u_z(r, t)$.

As for the momentum conservation equation, from the free body diagram depicted in Fig. 2, one can obtain the following relationship:

$$\begin{aligned} & p\pi\left((r + dr)^2 - r^2\right) - (p + dp)\pi\left((r + dr)^2 - r^2\right) \\ & + \rho\omega^2 z\pi\left((r + dr)^2 - r^2\right) dz + \tau(2\pi r) dz \\ & - (\tau + d\tau)(2\pi(r + dr)) dz \\ & = \rho\pi\left((r + dr)^2 - r^2\right) dz \frac{Du_z}{Dt}, \end{aligned} \quad (2)$$

where p , τ and D/Dt are pressure, shear stress and material derivative, respectively. Since u_z is a function of r and t only, Du_z/Dt becomes just the time derivative, $\partial u_z/\partial t$ and Eq. 2 can be reduced to

$$\rho \frac{\partial u_z}{\partial t} + \frac{1}{r} \tau + \frac{\partial \tau}{\partial r} = - \frac{\partial p}{\partial z} + \rho\omega^2 z. \quad (3)$$

For a Newtonian fluid case, the shear stress, with a sign convention defined in Fig. 2, can be expressed as

$$\tau(r, t) = -\mu \frac{\partial u_z}{\partial r}. \quad (4)$$

Then Eq. 3 becomes

$$\begin{aligned} \rho \frac{\partial u_z}{\partial t} - \mu \left(\frac{\partial^2 u_z}{\partial r^2} + \frac{1}{r} \frac{\partial u_z}{\partial r} \right) &= - \frac{\partial p}{\partial z} + \rho\omega^2 z, \\ \text{for } L_0 \leq z \leq l(t) \text{ and } t > 0. \end{aligned} \quad (5)$$

Equation 5 is a partial differential equation for velocity field, $u_z(r, t)$ and pressure field, $p(z, t)$. The domains of interest for z and t are also expressed in Eq. 5. It should be noted that the region occupied by the fluid is increasing as flow proceeds since $l(t)$ increases with the time, which is a peculiar nature of this transient flow. One might recognize that the domain of z at $t=0$ is null so that the velocity field is not defined at the time of $t=0$. In this regard, the conventional initial velocity of u_z is not to be considered in this study. Therefore, one has to solve Eq. 5 to obtain $u_z(r, t)$ and $p(z, t)$ just with appropriate boundary conditions. The boundary conditions are as follows:

$$u_z(r = R_h, t) = 0 \quad (\text{no-slip on the wall}) \quad (6a)$$

$$\left. \frac{\partial u_z(r, t)}{\partial r} \right|_{r=0} = 0 \quad (\text{symmetry of velocity profile}). \quad (6b)$$

and

$$p(L_0, t) = 0 \quad (7a)$$

$$p(l(t), t) = 0. \quad (7b)$$

Equation 7a indicates that the pressure head of the inlet reservoir is zero. The pressure head at the inlet is induced by the gravity force in the reservoir and the pressure at the inlet is generally much less than the viscous and centrifugal forces inside the microchannel. In this regard, we neglected the pressure head at the inlet to simplify the problem in the present study. The pressure at the flow front, i.e., at $z = l(t)$, is set to be zero in Eq. 7b by the assumption of neglecting the surface tension effect (Assumption 3).

In addition to the continuity and momentum equations, as a peculiar feature of this particular problem, one has to take into account the global mass conservation with regard to the flow front advancement. From the expression of the total flow rate, $Q(t)$, one can obtain the equation for the flow front advancement, namely $l(t)$, as below

$$Q(t) = \pi R_h^2 \frac{dl(t)}{dt} = \int_0^{R_h} 2\pi r u_z(r, t) dr, \quad (8)$$

the second part of the equation in Eq. 8 is the governing equation for $l(t)$ with the associated initial condition

$$l(t) = L_0 \quad \text{at } t = 0. \quad (9)$$

Once the velocity field is obtained, the flow advancement can be determined through Eq. 8.

In summary, one has to obtain analytic solutions for $u_z(r, t)$, $p(z, t)$ and $l(t)$ from Eqs. 5 and 8 with boundary conditions, Eqs. 6 and 7 and initial condition, Eq. 9.

4 Analytic solutions

In this section, we first manipulate the basic governing equations further to obtain more convenient forms of equations to deal with. Then we will introduce dimensionless forms of governing equations for the sake of understanding the nature of the flow more efficiently. From the dimensionless equations, we will derive two types of analytic solutions: (1) for a pseudostatic flow as an approximation of low Reynolds number-limiting case, and (2) for the general transient flow case as an exact solution.

Equation 5 can be recast to the following form,

$$\frac{\partial p}{\partial z} = \rho\omega^2 z - \left[\rho \frac{\partial u_z}{\partial t} - \mu \left(\frac{\partial^2 u_z}{\partial r^2} + \frac{1}{r} \frac{\partial u_z}{\partial r} \right) \right].$$

One can easily integrate the above equation with respect to z from L_0 to z at instant time t , recognizing that three terms in the bracket are independent of z , to result in

$$p(z, t) - p(L_0, t) = \frac{\rho\omega^2}{2}(z^2 - L_0^2) - \left[\rho \frac{\partial u_z}{\partial t} - \mu \left(\frac{\partial^2 u_z}{\partial r^2} + \frac{1}{r} \frac{\partial u_z}{\partial r} \right) \right] (z - L_0). \quad (10)$$

Substituting $l(t)$ for z in Eq. 10, along with boundary conditions of Eq. 7a and 7b at $z=L_0$ and $z=l(t)$, respectively, gives rise to an interesting equation as below,

$$\rho \frac{\partial u_z}{\partial t} - \mu \left(\frac{\partial^2 u_z}{\partial r^2} + \frac{1}{r} \frac{\partial u_z}{\partial r} \right) = \frac{\rho\omega^2}{2} (l(t) + L_0). \quad (11)$$

Making use of Eq. 11 and boundary condition of Eq. 7a, one can rewrite Eq. 10 as

$$p(z, t) = \frac{\rho\omega^2}{2} (z - L_0) (z - l(t)). \quad (12)$$

Now, in summary, the governing equations for $u_z(r, t)$ and $l(t)$ are Eqs. 11 and 8, respectively, along with boundary conditions, Eq. 6, and an initial condition, Eq. 9. Note that they are coupled with each other. Once $u_z(r, t)$ and $l(t)$ are known by solving them, one can calculate the pressure distribution from Eq. 12. It may be noted that Eq. 12 shows that pressure distribution is parabolic in the axial direction at any instant time t .

4.1 Dimensionless governing equations

Dimensionless form of equations would be more convenient to identify a group of dimensionless parameters which affect the flow rather than the dimensional form of equations, thus enabling one to gain the physical insight to the problem more clearly. In this regard, Eqs. 11 and 8 are nondimensionalized. For this purpose, we introduced characteristic quantities as listed below:

- Characteristic lengths: (1) R_h (hydraulic radius of the microchannel defined by $R_h = 2A_c/P$, where A_c and P are the cross-sectional area and perimeter of the microchannel, respectively) and (2) L (characteristic downchannel length, e.g., distance from the center of a CD plate to inlet reservoir)
- Characteristic velocities: (1) U (mean downchannel velocity of the fluid flow) and (2) V (rotational velocity defined by $V = L\omega_c$, where ω_c is the characteristic angular velocity)
- Characteristic times: (1) T_c (characteristic time for downchannel flow defined by $T_c = L/U$) and (2) $1/\omega_c$ (characteristic time for rotational motion defined by $1/\omega_c = L/V$)
- Characteristic pressure:

$$P_c = \frac{1}{2} \rho U^2$$

The dimensionless variables using such characteristic quantities are listed below:

$$r^* = \frac{r}{R_h}, \quad z^* = \frac{z}{L}, \quad t^* = \frac{t}{T_c} = \frac{tU}{L}, \quad (13)$$

$$\omega^* = \frac{\omega}{\omega_c} = \frac{\omega L}{V}, \quad u_z^*(r^*, t^*) = \frac{u_z(r, t)}{U},$$

$$p^*(z^*, t^*) = \frac{p(z, t)}{P_c} = \frac{2p}{(\rho U^2)}, \quad l^*(t^*) = \frac{l(t)}{L},$$

where superscript asterisk stands for corresponding dimensionless parameters.

Then, dimensionless form of Eq. 11 could be stated as,

$$-\frac{\partial^2 u_z^*}{\partial r^{*2}} - \frac{1}{r^*} \frac{\partial u_z^*}{\partial r^*} + ReA_R \frac{\partial u_z^*}{\partial t^*} = \frac{1}{2} ReA_R \bar{V}^2 \omega^{*2} (l^*(t^*) + L_0^*) \quad (14)$$

with the corresponding boundary conditions

$$u_z^*(1, t^*) = 0, \quad \left. \frac{\partial u_z^*(r^*, t^*)}{\partial r^*} \right|_{r^*=0} = 0, \quad (15)$$

where Re , A_R and \bar{V} denote the Reynolds number, $Re = \rho UR_h/\mu$, aspect ratio of hydraulic radius of microchannel to downchannel length, $A_R = R_h/L$, and ratio of rotational velocity to downchannel flow velocity, $\bar{V} = V/U$, respectively. It should be noted that the first two terms on the left-hand side of Eq. 14 represent the viscous force effect; the third term on the left-hand side expresses the inertia force effect; and the term on the right-hand side comes from the centrifugal (rotational) force effect. It is found from Eq. 14 that the two different dimensionless groups dominantly affect the fluid flow behavior: ReA_R and $\bar{V}\omega^*$. ReA_R represents the ratio of inertia force to viscous force, which enables us to estimate the inertia force effect on the flow system. $\bar{V}\omega^*$ is equal to $\omega L/U$, which is in fact the ratio of the rotational velocity of a disk to the downchannel flow velocity, associated with the centrifugal force as shown in Eq. 14.

Dimensionless form of Eq. 8 can be written as

$$Q^* = \frac{Q}{\pi R_h^2 U} = \frac{dl^*}{dt^*} = 2 \int_0^1 r^* u_z^* dr^* \quad (16)$$

with an initial condition

$$l^*(0) = L_0^*. \quad (17)$$

Finally, a dimensionless equation for pressure distribution was also derived from Eq. 12 as,

$$p^*(z^*, t^*) = \bar{V}^2 \omega^{*2} (z^* - L_0^*) (z^* - l^*(t^*)). \quad (18)$$

In summary, one has to solve $u_z^*(r^*, t^*)$ and $l^*(t^*)$ from the coupled Eqs. 14 and 16. Once they are solved, one can determine the pressure distribution from Eq. 18.

For most of the microfluidic applications, the fluid flow usually has a small Reynolds number due to the

small characteristic length of a microchannel. In this regard, we present two types of analytic solutions: (1) a pseudostatic approximate solution, which is corresponding to the relatively simple case when $ReA_R \ll 1$, and (2) an exact solution. It might be mentioned that the pseudostatic solution enables us to check the validity of the exact solution since the pseudostatic solution is corresponding to the asymptotic behavior of the exact solution as $ReA_R \rightarrow 0$.

4.2 Pseudostatic approximate solution

The microchannel flow usually has a small Re (i.e., $Re \ll 1$). The very small aspect ratio, A_R , also justifies $ReA_R \ll 1$, even when Re is relatively large. For the case of $ReA_R \ll 1$ while maintaining $ReA_R \bar{V}^2 \omega^{*2} \sim O(1)$, the effect of inertia force in Eq. 14 becomes negligible compared with the effects of viscous and centrifugal forces so that Eq. 14 can be reduced to

$$-\frac{\partial^2 u_z^*}{\partial r^{*2}} - \frac{1}{r^*} \frac{\partial u_z^*}{\partial r^*} = \frac{1}{2} ReA_R \bar{V}^2 \omega^{*2} (I^*(t^*) + L_0^*), \quad (19)$$

with the boundary conditions of Eq. 15, at instant time t^* . The solution of Eq. 19 is called the pseudostatic approximate solution since the inertia term does not play a role as if the viscous force were just balanced with the centrifugal force. It should be noted that the dimensionless velocity u_z^* is still a function of geometry, r^* , and time, t^* , although we neglect the inertia force term when $ReA_R \ll 1$.

From Eq. 19 with boundary conditions (Eq. 15), one can easily obtain a dimensionless velocity profile inside the circular microchannel,

$$u_z^*(r^*, t^*) = \frac{1}{8} ReA_R \bar{V}^2 \omega^{*2} (1 - r^{*2}) (I^*(t^*) + L_0^*). \quad (20)$$

Applying Eq. 20 to Eq. 16 yields the following equation for $I^*(t^*)$,

$$\frac{dI^*}{dt^*} = \frac{1}{16} ReA_R \bar{V}^2 \omega^{*2} (I^*(t^*) + L_0^*). \quad (21)$$

One can integrate Eq. 21 and apply the initial condition (Eq. 17) to obtain the final solution of a dimensionless pseudostatic flow front advancement, $I^*(t^*)$:

$$I^*(t^*) = L_0^* \left(2e^{\frac{1}{16} ReA_R \bar{V}^2 \omega^{*2} t^*} - 1 \right). \quad (22)$$

Equation 22 shows that the filled region of the microchannel exponentially increases with time, with $ReA_R \bar{V}^2 \omega^{*2}$ appearing as an exponent. The fluid flow front is thus strongly affected by ReA_R and $\bar{V}^2 \omega^{*2}$. The flow front is also found to be just proportional to L_0^* , the entrance location of microchannel.

Substitution of Eq. 22 to Eq. 20 gives the final solution of the dimensionless pseudostatic velocity profile:

$$u_z^*(r^*, t^*) = \frac{1}{4} ReA_R \bar{V}^2 \omega^{*2} L_0^* e^{\frac{1}{16} ReA_R \bar{V}^2 \omega^{*2} t^*} (1 - r^{*2}). \quad (23)$$

It is interesting to mention that the pseudostatic velocity profile of the centrifugal force-driven flow remains parabolic just like that of the pressure-driven flow and that the velocity increases exponentially with the time.

Finally, by substituting Eq. 22 to Eq. 18, one can obtain a final form of the dimensionless pseudostatic pressure distribution:

$$p^*(z^*, t^*) = \bar{V}^2 \omega^{*2} (z^* - L_0^*) \left(z^* + L_0^* - 2L_0^* e^{\frac{1}{16} ReA_R \bar{V}^2 \omega^{*2} t^*} \right). \quad (24)$$

In summary, for the given fluid properties, geometry of microchannel and processing conditions (i.e., rotational speed), one can determine the pseudostatic filling flow characteristics: filling flow front advancement, velocity profile and pressure distribution as the filling flow proceeds from Eqs. 22, 23 and 24, respectively.

4.3 Exact solution

In this section, we just present the exact solution to the coupled differential equations 14 and 16. One may refer to Appendix 1 for the detailed derivation of $I^*(t^*)$ and $u_z^*(r^*, t^*)$.

The exact solution of the dimensionless filling flow front advancement is found to be

$$I^*(t^*) = L_0^* [2e^{D t^*} - 1], \quad (25)$$

indicating that the filled region of the microchannel exponentially increases with the time as in the case of the pseudostatic approximation. The exponential growth rate is denoted by the exponent D which can be determined from the following nonlinear equation

$$\frac{D^2}{\bar{V}^2 \omega^{*2}} = \frac{1}{2} - \frac{1}{\sqrt{ReA_R D}} \frac{I_1^*(\sqrt{ReA_R D})}{I_0^*(\sqrt{ReA_R D})} \quad (26)$$

where I_0^* and I_1^* is the modified Bessel functions of the first kind, of order 0 and 1, respectively. It should be noted that the exponent D is the most important parameter to govern the centrifugal force-driven transient filling flow into the microchannel. D represents an inverse of a characteristic time indicating how fast the filling flow front into the microchannel advances: the higher the D is, the faster the flow front advances. Comparison between Eqs. 22 and 25 leads to the definition of D_{static} , exponential growth rate for the pseudostatic case as,

$$D_{\text{static}} = \frac{1}{16} ReA_R \bar{V}^2 \omega^{*2}. \quad (27)$$

The exact dimensionless velocity profile was also obtained as

$$u_z^*(r^*, t^*) = \frac{\bar{V}^2 \omega^{*2} L_0^*}{D} \left[1 - \frac{I_0^*(\sqrt{Re A_R D r^*})}{I_0^*(\sqrt{Re A_R D})} \right] e^{Dt^*}. \quad (28)$$

It is noted that the velocity profile of the exact case deviates from the parabolic shape of the pseudostatic approximation case. Furthermore, the dimensionless average velocity, $U_{\text{avg}}^*(t^*)$, can be obtained from Eqs. 16 and 25,

$$U_{\text{avg}}^*(t^*) = \frac{dI^*(t^*)}{dt^*} = 2DL_0^* e^{Dt^*}. \quad (29)$$

Finally, the exact dimensionless pressure distribution can be expressed as

$$p^*(z^*, t^*) = \bar{V}^2 \omega^{*2} (z^* - L_0^*) [z^* + L_0^* - 2L_0^* e^{Dt^*}] \quad (30)$$

In summary, for the given fluid properties, geometry of microchannel and processing conditions, one can calculate the exponent D through Eq. 26 and then determine the transient filling flow front advancement, velocity profile and pressure distribution as a function of time from Eqs. 25, 28 and 30, respectively.

Meanwhile, it may be noted that the asymptotic behaviors of the exact solutions (Eqs. 26, 25, 28 and 30) as $Re A_R \rightarrow 0$ are reduced to those of the pseudostatic case (Eqs. 27, 22, 23 and 24, respectively) while maintaining $Re A_R \bar{V}^2 \omega^{*2} \sim O(1)$, as they should. Proofs are provided in Appendix 2.

Finally, for the convenience of readers, we also summarized important results of the analytic solutions in a dimensional form in Appendix 3 since it is sometimes easier to understand the flow behavior if equations are expressed in a dimensional form rather than in a dimensionless form.

5 Analysis results and discussion

5.1 Parametric study for exponent D

As discussed above, the exponent D is the most important governing parameter in this transient flow, representing how fast the front of filling flow advances into the microchannel. In this regard, we will discuss the parametric study of D in this section.

As shown in Eq. 26, D is determined by two sets of dimensionless parameters, $Re A_R$ and $\bar{V} \omega^*$, which are associated with fluid properties, geometric data and processing conditions. Therefore, once $Re A_R$ and $\bar{V} \omega^*$ are determined from the information on sample fluid, microchannel geometry and processing conditions, it is rather straightforward to determine D by solving the nonlinear Eq. 26. For the parametric study, we extensively carried out computations of D for various combinations of $Re A_R$ and $\bar{V} \omega^*$.

Fig. 3 The calculated exponent D as a function of (a) $Re A_R$ and (b) $\bar{V} \omega^*$ (symbols from exact D , and curves from pseudostatic D_{static})

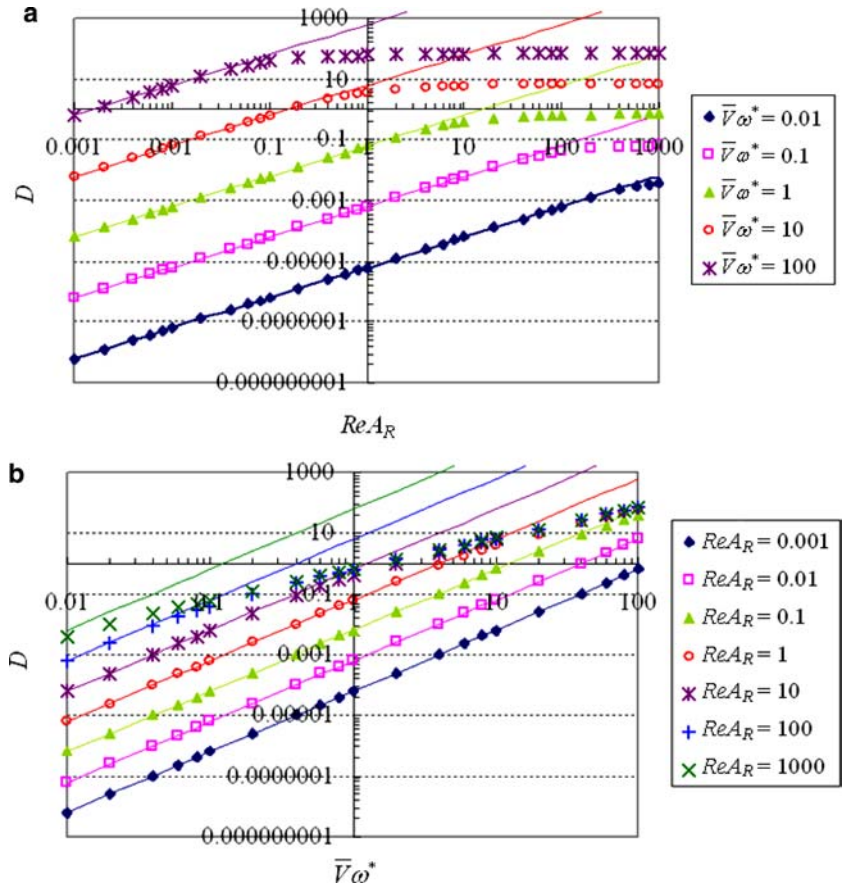


Figure 3 shows the calculated D for both pseudo-static (curves) and exact (symbols) cases as a function of ReA_R (Fig. 3a) and $\bar{V}\omega^*$ (Fig. 3b). Since D_{static} for the pseudo-static case is proportional to ReA_R and square of $\bar{V}\omega^*$ as expressed in Eq. 27, the D_{static} varies linearly for ReA_R and $\bar{V}\omega^*$ in logarithmic scale, which are represented as linear lines in Fig. 3a and b. It might be mentioned that the gap between the adjacent linear curves as shown in Fig. 3a (one order change of $\bar{V}\omega^*$) is wider than that of Fig. 3b (one order change of ReA_R) due to the square proportionality of D to $\bar{V}\omega^*$. Since D for the exact case asymptotically behaves like the pseudo-static D_{static} under the condition of $ReA_R \ll 1$ (Appendix 2), the calculated exact D lies on the lines of the pseudo-static D_{static} as shown in Fig. 3a and b while $ReA_R \ll 1$ even at high $\bar{V}\omega^*$, as expected. But, as ReA_R increases, the exact D becomes smaller than the pseudo-static D_{static} , which implies that the flow advancement in the exact solution is not as fast as the pseudo-static approximation case. This deviation is due to the inertia force effect (the third term in Eq. 14) which tends to restrain fluid mass from accelerating rapidly. As ReA_R increases further, the exact D deviates more and more from the curves of the pseudo-static D_{static} and

eventually approaches the limit value of $\bar{V}\omega^*/\sqrt{2}$ as $ReA_R \rightarrow \infty$, as clearly indicated in both Fig. 3a and b. Refer to Appendix 2 for the detailed derivation of this limit case of $ReA_R \rightarrow \infty$.

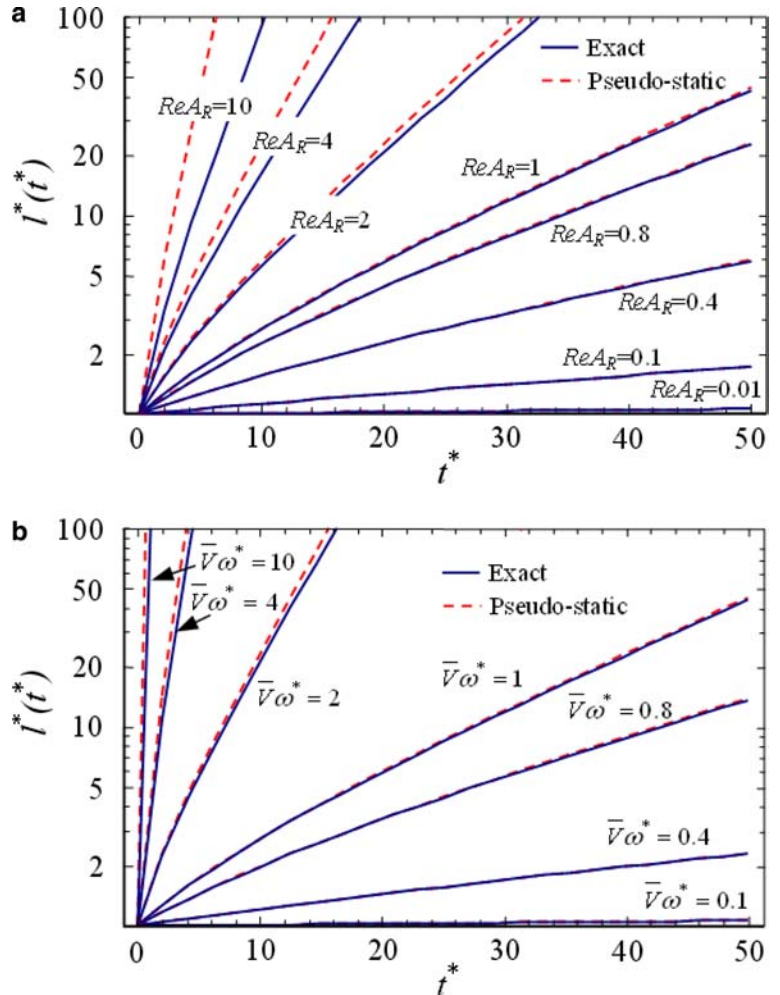
5.2 Parametric study for flow behavior

In order to provide a physical insight into the microfluidic system in this study, we extensively performed parametric studies on the flow behavior in terms of the flow front advancement, the velocity profile and the pressure distribution as functions of the time and various combinations of ReA_R and $\bar{V}\omega^*$.

5.2.1 Filling flow front advancement

Figure 4 shows the effects of ReA_R (Fig. 4a) and $\bar{V}\omega^*$ (Fig. 4b) on the behavior of the dimensionless filling flow front advancement, l^* (t^*), with respect to dimensionless time, t^* , for both the pseudo-static (dotted curves) and exact (solid curves) cases. For the case of Fig. 4a, various values of ReA_R are chosen: 0.01, 0.1,

Fig. 4 Filling flow front advancements for both cases of the pseudo-static (dotted curves) and exact (solid curves) solutions with respect to the variation of time: **a** effect of ReA_R and **b** effect of $\bar{V}\omega^*$



0.4, 0.8, 1, 2, 4 and 10 when $L_0^* = 1$ and $\bar{V}\omega^* = 1$. The pseudostatic D_{static} corresponding to those values of ReA_R are found to be 0.000625, 0.00625, 0.025, 0.05, 0.0625, 0.125, 0.25 and 0.625, respectively, from Eq. 27, and exact D corresponding to them are 0.000625, 0.00624935, 0.0249585, 0.0496711, 0.0618624, 0.120191, 0.218354 and 0.383823, respectively (Eq. 26). And, for the case of Fig. 4b, we vary the values of $\bar{V}\omega^*$ as 0.1, 0.4, 0.8, 1, 2, 4 and 10 while maintaining $L_0^* = 1$ and $ReA_R = 1$. The values of pseudostatic D_{static} corresponding to these $\bar{V}\omega^*$ s become 0.000625, 0.01, 0.04, 0.0625, 0.25, 1 and 6.25, respectively, and the exact D are 0.000624925, 0.00998339, 0.0397368, 0.0618624, 0.240381, 0.873416 and 3.83823, respectively.

It is noted that l^* (t^*) shows, in the logarithmic scale of the ordinate, a nonlinear behavior near $t^* = 0$ due to the term -1 inside the bracket of Eqs. 22 and 25, as plotted in Fig. 4a, b. However, as t^* is sufficiently large, the term, -1 becomes negligible in comparison with the exponential term of $2e^{Dr^*}$, and therefore l^* (t^*) shows a linear behavior in the logarithmic scale of the ordinate. It might also be noted that since the values of pseudostatic D_{static} and the exact D are almost the same at small ReA_R and $\bar{V}\omega^*$, the curves of pseudostatic and exact l^* (t^*) almost coincide with each other.

As clearly shown in Fig. 4, the behavior of l^* (t^*) is more sensitively affected by the change of $\bar{V}\omega^*$ than ReA_R due to the fact that the exponent D is proportional to the square of $\bar{V}\omega^*$ while it is linearly proportional to ReA_R . Meanwhile, as ReA_R increases, the deviation between the pseudostatic and exact cases gets larger as indicated in Fig. 4a, due to the inertia force effect as discussed earlier. On the other hand, Fig. 4b shows a very small deviation between the pseudostatic and exact cases due to a relatively small ReA_R (in this case, $ReA_R = 1$).

5.2.2 Velocity profile

Plotted in Fig. 5 are typical behaviors of velocity profile with respect to (a) t^* , (b) ReA_R and (c) $\bar{V}\omega^*$ for both cases of pseudostatic (dotted curves) and exact (solid curves) solutions. Figure 5a shows the typical velocity profile development according to the increase of time (in this case $t^* = 20, 40, 60, 80$ and 100) for a specific case of $ReA_R = 10$ and $\bar{V}\omega^* = 0.2$ with $L_0^* = 1$. The corresponding pseudostatic D_{static} and exact D are 0.025 and 0.0240381, respectively. The pseudostatic flow keeps the parabolic velocity profiles, like those of a pressure-driven flow. But the maximum velocity exponentially increases with the time as expressed in Eq. 23. Since the flow front position gets exponentially away from the center with the time as illustrated in Fig. 4, the induced centrifugal force which is a flow driving force in the system exponentially increases with the time, resulting in the exponential increase of maximum velocity. It is noted that due to a smaller value of D than the pseudo-

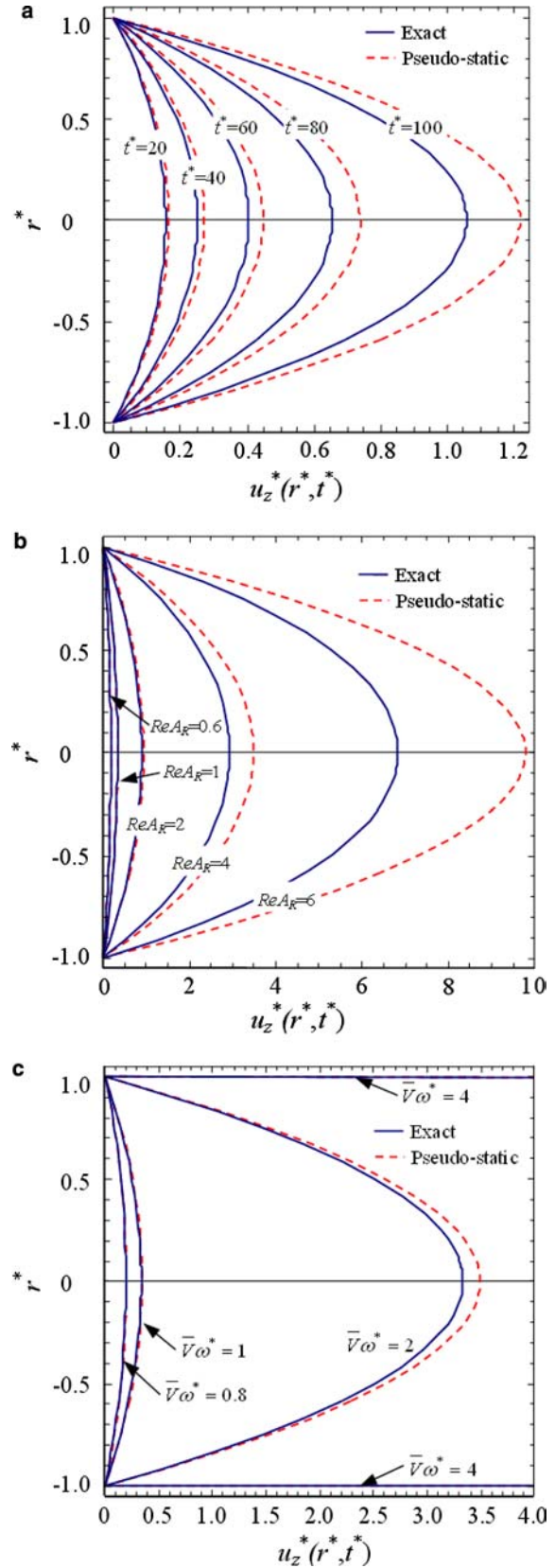
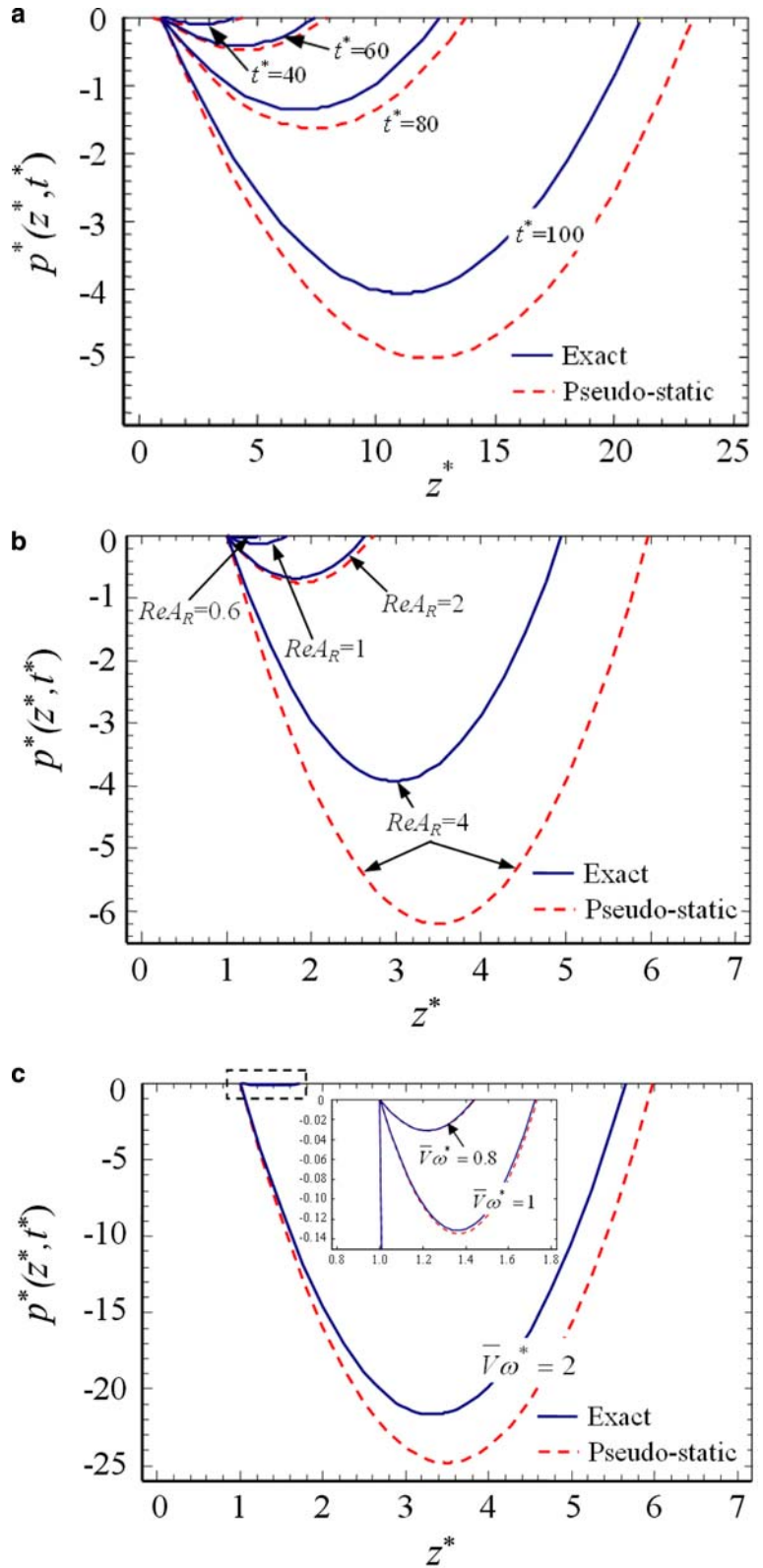


Fig. 5 The change of velocity profile for both cases of pseudostatic (dotted curves) and exact (solid curves) solutions with respect to the variation of **a** dimensionless time, t^* , **b** ReA_R and **c** $\bar{V}\omega^*$

Fig. 6 The change of pressure distribution for both cases of pseudostatic (*dotted curves*) and exact (*solid curves*) solutions with respect to the variation of a dimensionless time, t^* , **b** ReA_R and **c** $\bar{V}\omega^*$. *Inset* in **c** shows an enlarged view of the dashed area



static D_{static} , the exact velocity profile is getting smaller than the pseudostatic one as time proceeds. In other words, since the inertia force restrains the rapid velocity increase, the real velocity profile development becomes

more deviated from the pseudostatic case with the time even at $ReA_R = 10$.

The variations of velocity profile in response to ReA_R and $\bar{V}\omega^*$ are shown in Fig. 5b and c, respectively, for

both cases of pseudostatic (dotted curves) and exact (solid curves) solutions at the same instant time, $t^* = 5$. In Fig. 5b, ReA_R varies as 0.6, 1, 2, 4 and 6 when $L_0^* = 1$ and $\bar{V}\omega^* = 1$. The corresponding calculated pseudostatic D_{static} are 0.0375, 0.0625, 0.125, 0.25 and 0.375, respectively, and exact D are 0.0373604, 0.0618624, 0.120191, 0.218354 and 0.291029, respectively. For the case of Fig. 5c, $\bar{V}\omega^*$ varies as 0.8, 1, 2 and 4 when $L_0^* = 1$ and $ReA_R = 1$. The corresponding pseudostatic D_{static} are calculated as 0.04, 0.0625, 0.25 and 1, respectively, and exact D are 0.0397368, 0.0618624, 0.240381 and 0.873416, respectively. Due to the dependency of the exponent D on square of $\bar{V}\omega^*$, the velocity profile is more sensitively affected by the change of $\bar{V}\omega^*$ (Fig. 5c) than ReA_R (Fig. 5b). However, it is noted that the higher the ReA_R is, the more the deviation between the pseudostatic and exact cases, which is the same trend as l^* (t^*), due to the inertia force effect restraining a rapid velocity increase. It might be mentioned that Fig. 5c plots the velocity profile only in the vicinity of the wall for the case of $\bar{V}\omega^* = 4$ since the velocity magnitude in the other region exceeds the given range of the ordinate.

5.2.3 Pressure distribution

Plotted in Fig. 6 are typical pressure distributions with respect to (a) t^* , (b) ReA_R and (c) $\bar{V}\omega^*$ for both cases of pseudostatic (dotted curves) and exact (solid curves) solutions. Figure 6a shows the typical development of the pressure distribution as time increases (in this case $t^* = 40, 60, 80$ and 100) for a specific case of $ReA_R = 10$ and $\bar{V}\omega^* = 0.2$ with $L_0^* = 1$. The corresponding pseudostatic D_{static} and exact D are calculated as 0.025 and 0.0240381, respectively. As expected from Eq. 18, both the pseudostatic and exact pressure distributions show parabolic shapes and negative value of pressure over the microchannel. The first zero pressure of one fixed end point of the parabola represents the starting position, i.e., the reservoir, L_0^* , (in this case, $L_0^* = 1$), and the second zero pressure of the other moving end point corresponds to the filling flow front, i.e., the advancing position of flow front, l^* (t^*), at the indicated time, t^* . Due to the difference of the pseudostatic D_{static} and exact D , the positions of the second zero pressure point at the same instant time deviate more and more from each other as time proceeds. The filled portion of a microchannel could be divided to two distinctive regions: (1) the left half region from the starting point (the reservoir) to the center (the center of filled region inside the microchannel at the indicated time) having a negative pressure gradient; (2) the right half region from the center to the other second end point (the position of the filling flow front) showing a positive pressure gradient. At the center of the filled channel, i.e., between the two regions, the pressure gradient is zero. These trends can be explained by the force balance between the centrifugal force, pressure gradient and the shear stress based on the assumptions

in this study. It might be reminded that the velocity component, u_z , is a function of r only (not z) at any instant time, thus the shear stress becomes a function of r only at an instant time, thus remaining the same over the entire filled region of the microchannel. The centrifugal force linearly increases with the radial location of the CD plate. In response to the increasing centrifugal force with the radial direction, the pressure is developed to maintain the same shear force throughout the filled region inside the microchannel as follows. A small centrifugal force in the left half region needs a negative pressure gradient (a favorable pressure gradient to the flow), while a positive pressure gradient (an adverse pressure gradient to the flow) should compensate for a large centrifugal force in the right half region, in order to match exactly the average centrifugal force (with zero pressure gradient) at the center. This is how a parabolic and negative pressure distribution is built up in the microchannel.

Figure 6b, c shows the pressure distributions with regard to the change of ReA_R and $\bar{V}\omega^*$, respectively, for both the pseudostatic (dotted curves) and exact (solid curves) solutions at the same instant time, $t^* = 5$. For the case of Fig. 6b, ReA_R varies as 0.6, 1, 2 and 4 when $L_0^* = 1$ and $\bar{V}\omega^* = 1$. The corresponding pseudostatic D_{static} are 0.0375, 0.0625, 0.125 and 0.25, respectively, and exact D are 0.0373604, 0.0618624, 0.120191 and 0.218354, respectively. In Fig. 6c, $\bar{V}\omega^*$ varies as 0.8, 1 and 2 when $L_0^* = 1$ and $ReA_R = 1$. The corresponding pseudostatic D_{static} are calculated as 0.04, 0.0625 and 0.25, respectively, and exact D are 0.0397368, 0.0618624 and 0.240381, respectively. Like the change of velocity profile, the pressure distribution is more sensitively influenced by the change of $\bar{V}\omega^*$ (Fig. 6c) than ReA_R (Fig. 6b). And the higher ReA_R is, the more deviation one can observe between the pseudostatic and exact pressure distributions as explained above.

Finally, we want to comment on the limitations and potentials of the modeling and analysis developed in this study with respect to applications. First, we neglected the Coriolis force in obtaining the analytic solutions of this transient filling flow problem. This assumption is valid under the relatively low rotational speed, e.g., below 1,000 rpm with a typical microchannel size of the order of 100 μm . The analytic solutions presented in this study may not be accurate at a very high rotational speed. However, the analytic solutions still enables us to get a physical insight into the centrifugal force-driven fluid flow and help us design such a microchannel system for a wide range of a rotational speed. One may refer to Appendix 4 for the detailed magnitude analysis for the centrifugal force and the Coriolis force. Second, we neglected surface tension effect at the boundary of the flow front. As discussed before, if one applies a plastic substrate of which the contact angle of sample liquid is nearly 90° , the assumption is valid. When the surface tension plays an essential role in the hydrophilic/phobic fluidic con-

trol, incorporating the surface tension effect into the analytic approach might become important. In this regard, we are currently investigating the effect of surface tension in the context of the present model problem, which will be the subject of a separate paper in the future.

6 Design application examples

As already described above, one of the principal objectives of this work is to provide a simple analytic design tool at the first design step. In this regard, we present two different application examples as typical design problems in which the hydraulic radius of a microchannel or the processing condition of rotational speed is determined so as to meet the design requirements by means of the results of modeling and analysis performed in this study.

Suppose a microfluidic designer wants to deliver a sample fluid from the reservoir location, L_0 , to the desired radial downchannel location, L_d , at a desired time, t_d . There are two possible design cases: (1) case I, where one has to design the hydraulic radius for a new microfluidic system to be fabricated with a specific rotational speed of a disk-driving system already fixed, and (2) case II, where one has to determine a rotational speed of a disk with a given hydraulic radius in an existing microfluidic system fabricated already.

To meet the design requirement, one can use the following design equations in sequence. *The first design equation* can be obtained by rearranging Eq. 60 in Appendix 3 as follows:

$$\text{Design equation I: } D = \frac{1}{t_d} \ln \left[\frac{1}{2} \left(\frac{L_d}{L_0} + 1 \right) \right] \quad (31)$$

which is to determine a dimensional value of D for the given values of L_d , L_0 and t_d . And *the second design equation* is Eq. 63 in Appendix 3 as duplicated below:

$$\text{Design equation II: } \frac{R_h^2}{\omega^2} D^2 = \frac{R_h^2}{2} - \sqrt{\frac{\mu}{D\rho}} R_h \frac{I_1 \left(\sqrt{\frac{D\rho}{\mu}} R_h \right)}{I_0 \left(\sqrt{\frac{D\rho}{\mu}} R_h \right)} \quad (32)$$

from which the hydraulic radius, R_h , or the rotational speed, ω , is subsequently determined for given conditions with the calculated D .

As a specific design example, let the sample fluid properties and design requirements be as follows:

- Fluid properties: $\rho = 10^3 \text{ kg m}^{-3}$ and $\mu = 10^{-3} \text{ Pa s}$, which are the same order as those of water
- Position of reservoir (i.e., entrance location of microchannel): $L_0 = 5 \text{ mm}$
- Design requirements: $L_d = 40 \text{ mm}$ and $t_d = 2 \text{ s}$.
- Therefore, for the given values of L_d , L_0 and t_d , D is determined as $D = 0.752 \text{ s}^{-1}$ from *Design Eq. I*,

Eq. 31. Then, depending on the design case, one can determine the other parameter as below

6.1 Case I: determine R_h for a given rotational speed, ω

Suppose that a designer wants to deliver the sample to the desired radial position on a CD plate which is rotated with a specific rotational speed, ω . This problem is typically encountered at the design step.

If the CD is rotated with $\omega = 40 \text{ rad s}^{-1} \approx 382 \text{ rpm}$, the corresponding hydraulic radius can be determined through *Design Eq. II*, Eq. 32 as $R_h = 86.8 \text{ }\mu\text{m}$.

6.2 Case II: determine ω for a given hydraulic radius, R_h , of a microchannel

The cross-sectional area of microchannel may be given already in an existing microfluidic system or may be first assigned in the design step of a new system especially when the sample volume to be delivered is specifically given. The sample fluid can be delivered to the desired radial position at a desired time by adjusting the rotational speed. This problem is typically encountered at the experimental step.

If the hydraulic radius of a microchannel on the CD plate is assigned to (or given by) $R_h = 100 \text{ }\mu\text{m}$, the corresponding rotational speed can be determined as $\omega = 34.72 \text{ rad s}^{-1} \approx 330 \text{ rpm}$ from *Design Eq. II*, Eq. 32.

As illustrated through Cases I and II, a microfluidic designer can determine the hydraulic radius of microchannel or the rotational speed for given experimental conditions and design requirements by means of *Design Eqs. I and II* (Eqs. 31, 32).

7 Concluding remarks

In this paper, we have first developed the physical modeling and carried out the analysis for the transient filling flow into the circular microchannel driven by centrifugal force. By means of the modeling and analysis, we have successfully provided not only a physical insight into such a microchannel flow but also a simple design tool.

The governing equations for the filling flow were developed from the fundamental force balance (among viscous force, inertia force and centrifugal force) for an infinitesimal control volume in the microchannel together with the continuity equation. With the developed physical modeling in a dimensionless form, first, a pseudostatic approximate solution was derived for the case when the inertia force is negligible, and secondly, an exact analytic solution was derived with the inertia force effect included.

The analytic results showed that the filled region into the microchannel exponentially increases with the time

for the centrifugal force-driven filling flow. The transient flow behavior is very sensitively affected by the dimensionless parameters of $\bar{V}\omega^*$ (associated with the centrifugal force effect) and ReA_R (related with the inertia force effect) which are combinations of fluid properties, microchannel geometries and processing conditions.

The exponent D which represents an inverse of a characteristic time for flow front advancement, i.e., indicating how fast the microchannel is filled, is found to be the most important parameter in this study. The parametric study on D showed that the filling flow behavior is more sensitively influenced by the change of $\bar{V}\omega^*$ than ReA_R since D is proportional to the square of $\bar{V}\omega^*$ and linearly proportional to ReA_R . And as ReA_R increases, the inertia force effect becomes more important in the system, resulting in the increase of the deviation between the pseudostatic approximation solution and exact one since the inertia force effect tends to restrain flow velocity from a rapid acceleration.

The parametric studies on filling flow front advancement, $l^*(t^*)$, velocity profile, $u_z^*(r^*, t^*)$ and pressure distribution, $p^*(z^*, t^*)$, were also carried out to understand the flow behavior. All $l^*(t^*)$, $u_z^*(r^*, t^*)$ and $p^*(z^*, t^*)$ are more sensitively affected by the change of $\bar{V}\omega^*$ than ReA_R as expected from the behavior of D . It is also expected that the higher the ReA_R induces the larger the deviation between the pseudostatic and exact solutions for all three flow characteristic variables. It is noted that the velocity profile of the pseudostatic case is parabolic like the pressure-driven flow and that the inertia force makes the exact velocity profile deviated from the parabolic profile. The pressure is negative and has a parabolic distribution along the downchannel direction for both pseudostatic and exact cases so as to maintain the force balance in the filled region of a microchannel.

With regard to the design tool for the system, two design equations have been proposed and two types of design application examples are demonstrated successfully. By means of two design equations, a microfluidic designer can easily determine the hydraulic radius of a microchannel or the rotational speed to meet the design requirements for given conditions.

As a final remark, this study might become a platform for the analytic approaches not only for an arbitrary channel path but also for a complex microchannel network system in which the fluid flow is driven by centrifugal force.

Acknowledgements The authors would like to thank the Korean Ministry of Science and Technology for the financial supports via the National Research Laboratory Program (2000-N-NL-01-C-148) and the Korean Ministry of Education & Human Resources Development supporting BK21 program. Partial support from the Korean Ministry of Commerce, Industry and Energy via a research project of Micro-Injection/Compression Molding Technology for Polymer-based Micro-Parts is also appreciated. The authors also thank Dr. Chong H. Ahn of University of Cincinnati for helpful technical discussion.

Appendix 1

Detailed solution procedures for dimensionless exact filling flow front advancement, $l^*(t^*)$, and dimensionless exact velocity profile, $u_z^*(r^*, t^*)$

The governing equation for $u_z^*(r^*, t^*)$ and the corresponding boundary conditions are stated in Eqs. 14 and 15, respectively. And the governing equation for $l^*(t^*)$ and the corresponding initial condition are written in Eqs. 16 and 17, respectively. Equations 14 and 16 are coupled with each other.

For this particular problem, the separation of variable technique turns out to be successful to lead to an exact solution with the following form

$$u_z^*(r^*, t^*) = U_z^*(r^*)T^*(t^*), \quad (33)$$

where U_z^* and T^* are geometrical and temporal velocity components which are the functions of r^* only and t^* only, respectively. With the solution form of Eqs. 33, 14 can be rewritten by

$$\begin{aligned} -\left[\frac{d^2U_z^*}{dr^{*2}} + \frac{1}{r^*}\frac{dU_z^*}{dr^*}\right]T^* + ReA_RU_z^*\frac{dT^*}{dt^*} \\ = \frac{1}{2}ReA_R\bar{V}^2\omega^{*2}(l^*(t^*) + L_0^*). \end{aligned} \quad (34)$$

Observing that the right-hand side in Eq. 34 is the function of t^* only, i.e., independent of r^* , one can decompose the left-hand side of Eq. 34 by functions of r^* and t^* so that the part of the function of r^* only could set to be constant. With this in mind, the following relation is assumed

$$\frac{dT^*}{dt^*} = AT^*(t^*) \quad (35)$$

where A is constant. Then from Eqs. 34 and 35, one can obtain the following equations

$$-\frac{d^2U_z^*}{dr^{*2}} - \frac{1}{r^*}\frac{dU_z^*}{dr^*} + ReA_RA U_z^* = B \quad (36)$$

$$BT^*(t^*) = \frac{1}{2}ReA_R\bar{V}^2\omega^{*2}(l^*(t^*) + L_0^*) \quad (37)$$

where B is constant.

By substituting Eqs. 33 and 37 to the governing equation for $l^*(t^*)$, Eq. 16, one can obtain the following equation:

$$\frac{dl^*}{dt^*} = ReA_R\bar{V}^2\omega^{*2}(l^*(t^*) + L_0^*) \int_0^1 r^* \frac{U_z^*(r^*)}{B} dr^*. \quad (38)$$

We define the constant part by D as follows

$$D \equiv ReA_R \bar{V}^2 \omega^{*2} \int_0^1 r^* \frac{U_z^*(r^*)}{B} dr^*. \quad (39)$$

Then Eq. 38 is rewritten as

$$\frac{dI^*}{dt^*} = D(I^*(t^*) + L_0^*). \quad (40)$$

By applying the initial condition of Eq. 17, one attains a final form of the dimensionless exact filling flow front advancement

$$I^*(t^*) = L_0^* [2e^{Dt^*} - 1] \quad (41)$$

which corresponds to Eq. 25.

From Eqs. 37 and 41, one can find $T^*(t^*)$ as

$$T^*(t^*) = \frac{1}{B} ReA_R \bar{V}^2 \omega^{*2} L_0^* e^{Dt^*} \quad (42)$$

Since Eq. 42 holds, one can recognize that Eq. 35 is satisfied if A appearing in Eq. 35 is no more than D defined in Eq. 39, i.e.,

$$A = D. \quad (43)$$

Reflecting Eq. 43, one can rewrite Eq. 36 as

$$-\frac{d^2 U_z^*}{dr^{*2}} - \frac{1}{r^*} \frac{dU_z^*}{dr^*} + ReA_R D U_z^* = B \quad (44)$$

which is the differential equation for the geometrical (spatial) velocity component to be solved along with the boundary conditions,

$$U_z^*(r^* = 1) = 0 \quad (\text{no-slip on the wall}) \quad (45)$$

$$\left. \frac{dU_z^*}{dr^*} \right|_{r^*=0} = 0 \quad (\text{symmetry of velocity profile}). \quad (46)$$

It may be mentioned that Eq. 44 becomes an integro-differential equation for U_z^* if D defined in Eq. 39 is explicitly substituted to Eq. 44. This integro-differential equation is difficult to be solved analytically. Thus, in the present approach, we regard Eq. 44 as a differential equation just for U_z^* considering D as a parameter given, even if D could be determined only after U_z^* is solved.

It is rather straightforward to solve Eq. 44 which has a standard differential equation form of the modified Bessel function of order zero. The solution $U_z^*(r^*)$ includes a homogeneous solution part, $U_{z,h}^*(r^*)$, and a particular solution part, $U_{z,p}^*(r^*)$, as follows,

$$\begin{aligned} U_z^*(r^*) &= U_{z,h}^*(r^*) + U_{z,p}^*(r^*) \\ &= c_1 I_0^*(\sqrt{ReA_R D} r^*) + c_2 K_0^*(\sqrt{ReA_R D} r^*) \\ &\quad + \frac{B}{ReA_R D} \end{aligned} \quad (47)$$

where I_0^* and K_0^* are the modified Bessel function of order zero of the first kind and second kind, respectively, and c_1 and c_2 are integral constants. By applying boundary conditions of Eqs. 45, 46, one attains the final solution of $U_z^*(r^*)$ as

$$U_z^*(r^*) = \frac{B}{ReA_R D} \left[1 - \frac{I_0^*(\sqrt{ReA_R D} r^*)}{I_0^*(\sqrt{ReA_R D})} \right]. \quad (48)$$

Finally, from Eqs. 33, 42 and 48, the dimensionless exact velocity field is expressed as

$$u_z^*(r^*, t^*) = \frac{\bar{V}^2 \omega^{*2} L_0^*}{D} \left[1 - \frac{I_0^*(\sqrt{ReA_R D} r^*)}{I_0^*(\sqrt{ReA_R D})} \right] e^{Dt^*} \quad (49)$$

which corresponds to Eq. 28.

Now to complete the solution, one needs an expression for D . By substituting Eq. 48 to Eq. 39, one can obtain the following relation for D ,

$$\frac{D^2}{\bar{V}^2 \omega^{*2}} = \frac{1}{2} - \frac{1}{\sqrt{ReA_R D}} \frac{I_1^*(\sqrt{ReA_R D})}{I_0^*(\sqrt{ReA_R D})} \quad (50)$$

which corresponds to Eq. 26. I_1^* is the modified Bessel function of the first kind, of order one.

Appendix 2

Asymptotic behaviors of exact solutions

The asymptotic behaviors of the exact solutions (Eqs. 26, 25, 28 and 30) as $ReA_R \rightarrow 0$ must be reduced to those of the pseudostatic case (Eqs. 27, 22, 23 and 24, respectively) while maintaining $ReA_R \bar{V}^2 \omega^{*2} \sim O(1)$, as they should.

First, the expression for D , Eq. 26, can be rewritten by introducing the infinite series expansion form of the modified Bessel functions of I_0^* and I_1^* as,

$$\frac{D^2}{\bar{V}^2 \omega^{*2}} = \frac{1}{2} - \frac{1}{\sqrt{ReA_R D}} \frac{\frac{1}{2} \sqrt{ReA_R D} + \frac{1}{16} (ReA_R D)^{3/2} + \frac{1}{384} (ReA_R D)^{5/2} + O((ReA_R D)^{7/2})}{1 + \frac{1}{4} ReA_R D + \frac{1}{64} (ReA_R D)^2 + O((ReA_R D)^3)}. \quad (51)$$

Rearranging Eq. 51 with regard to D results in

$$\begin{aligned} \frac{1}{32} Re^2 A_R^2 D^3 + \frac{1}{2} Re A_R D^2 + \left(2 - \frac{1}{96} (Re A_R)^2 \bar{V}^2 \omega^{*2}\right) D \\ = \frac{1}{8} Re A_R \bar{V}^2 \omega^{*2}. \end{aligned} \quad (52)$$

If $Re A_R \ll 1$ while $Re A_R \bar{V}^2 \omega^{*2} \sim O(1)$. Equation 52 can be reduced to an expression for D as

$$D = \frac{1}{16} Re A_R \bar{V}^2 \omega^{*2} \quad (53)$$

which is identical to the pseudostatic D_{static} , Eq. 27. And consequently, the filling flow front advancement, Eq. 25, and pressure distribution of the exact case, Eq. 30, become the exactly same as those of the pseudostatic case, Eqs. 22 and 24, respectively.

Expanding $I_0^*(\sqrt{Re A_R D} r^*)$ and $I_0^*(\sqrt{Re A_R D})$ by means of the infinite series form in the exact velocity profile, Eq. 28, results in

$$\begin{aligned} u_z^*(r^*, t^*) \\ = \frac{\bar{V}^2 \omega^{*2} L_0^*}{D} \left[1 - \frac{1 + \frac{1}{4} Re A_R D r^{*2} + O\left((Re A_R D r^*)^2\right)}{1 + \frac{1}{4} Re A_R D + O\left((Re A_R D)^2\right)} \right] e^{Dr^*}. \end{aligned} \quad (54)$$

Due to $1 \gg (1/4) Re A_R D$ under the assumption of $Re A_R \ll 1$, the above equation could be reduced to

$$u_z^*(r^*, t^*) \approx \frac{1}{4} Re A_R \bar{V}^2 \omega^{*2} L_0^* (1 - r^{*2}) e^{Dr^*}. \quad (55)$$

With D in Eqs. 53, 55 becomes identical to Eq. 23 of the pseudostatic case.

Therefore, the asymptotic behavior of the exact solutions are proved to be completely identical to those of the pseudostatic approximate solutions when $Re A_R \rightarrow 0$ while maintaining $Re A_R \bar{V}^2 \omega^{*2} \sim O(1)$.

Finally, we further investigate the asymptotic behavior of the exponent D as $Re A_R \rightarrow \infty$. From the infinite series expansion of I_0^* and I_1^* , one can show that $I_1^*(\sqrt{Re A_R D})/I_0^*(\sqrt{Re A_R D}) \rightarrow 0$ as $Re A_R \rightarrow \infty$. Therefore, from Eq. 26, the exact exponent D is found to deviate from the pseudostatic D_{static} and to approach a limit value of $\bar{V} \omega^*/\sqrt{2}$ as $Re A_R \rightarrow \infty$, which is shown in Fig. 3a, b.

Appendix 3

Solutions in dimensional form

Dimensional forms of the pseudostatic solutions are expressed below

A pseudostatic filling flow front advancement, $l(t)$, corresponding to Eq. 22:

$$l(t) = L_0 \left[2 \exp \left[\left(\frac{\rho \omega^2 R_h^2}{16 \mu} t \right) \right] - 1 \right]. \quad (56)$$

A pseudostatic velocity profile, corresponding to Eq. 23

$$u_z(r, t) = \frac{\rho \omega^2 L_0}{4 \mu} \exp \left[\left(\frac{\rho \omega^2 R_h^2}{16 \mu} t \right) \right] (R_h^2 - r^2). \quad (57)$$

A pseudostatic pressure distribution, corresponding to Eq. 24

$$p(z, t) = \frac{\rho \omega^2}{2} (z - L_0) \left[z + L_0 - 2L_0 \exp \left[\left(\frac{\rho \omega^2 R_h^2}{16 \mu} t \right) \right] \right]. \quad (58)$$

A dimensional form of D_{static} , corresponding to Eq. 27

$$D_{\text{static}} = \frac{\rho \omega^2 R_h^2}{16 \mu}. \quad (59)$$

Dimensional forms of the exact solutions are expressed below. An exact filling flow front advancement, $l(t)$, corresponding to Eq. 25

$$l(t) = L_0 [2e^{Dt} - 1]. \quad (60)$$

An exact velocity profile, corresponding to Eq. 28

$$u_z(r, t) = \frac{L_0 \omega^2}{D} \left[1 - \frac{I_0 \left(\sqrt{\frac{D \rho}{\mu}} r \right)}{I_0 \left(\sqrt{\frac{D \rho}{\mu}} R_h \right)} \right] e^{Dt}. \quad (61)$$

An exact pressure distribution, corresponding to Eq. 30

$$p(z, t) = \frac{\rho \omega^2}{2} (z - L_0) [(z + L_0) - 2L_0 e^{Dt}]. \quad (62)$$

A dimensional form of D , corresponding to Eq. 26

$$\frac{R_h^2}{\omega^2} D^2 = \frac{R_h^2}{2} - \sqrt{\frac{\mu}{D \rho}} R_h \frac{I_1 \left(\sqrt{\frac{D \rho}{\mu}} R_h \right)}{I_0 \left(\sqrt{\frac{D \rho}{\mu}} R_h \right)}. \quad (63)$$

Appendix 4

Comparison between the Coriolis force and the centrifugal force

The ratio of the centrifugal force to the Coriolis force corresponding to the characteristic dimensions defined in this study be stated as follows:

$$\frac{\text{Centrifugal force}}{\text{Coriolis force}} = \frac{\rho \omega_c^2 L}{2 \rho U \omega_c} = \frac{\omega_c L}{2U} = \frac{V}{2U} = \frac{\bar{V}}{2}. \quad (64)$$

This result indicates that the ratio of the centrifugal force to the Coriolis force is equal to half the ratio of the rotational velocity (V) to the mean downchannel velocity (U), $\bar{V}/2$. Therefore, if \bar{V} is large enough, one can neglect the Coriolis force effect.

One can roughly estimate the mean downchannel velocity, U , by equalizing the viscous force to the centrifugal force, that is,

$$\mu \frac{U}{R_h^2} = \rho \omega_C^2 L. \quad (65)$$

Then one can obtain the following estimation of U :

$$U = \frac{\rho \omega_C^2 L R_h^2}{\mu}. \quad (66)$$

Thus the force ratio of Eq. 64 becomes

$$\frac{\text{Centrifugal force}}{\text{Coriolis force}} = \frac{V}{2U} = \frac{\mu}{2\rho\omega_C R_h^2}. \quad (67)$$

From Eq. 67, it is found that as the rotational speed (ω_C) increases, the Coriolis force effect becomes important. However, the effect of the Coriolis force becomes negligible as the microchannel radius (R_h) and the density (ρ) decrease, and as the viscosity (μ) increases.

As a specific example with the real values, let the sample fluid properties and microchannel geometry be as follows:

Fluid properties $\rho = 10^3 \text{ kg m}^{-3}$ and $\mu = 10^{-3} \text{ Pa s}$

Radius of microchannel $R_h = 50 \text{ }\mu\text{m}$.

Then, according to Eq. 67 the force ratio is determined as

$$\frac{\text{Centrifugal force}}{\text{Coriolis force}} = \frac{\bar{V}}{2} = \frac{200}{\omega_C}. \quad (68)$$

Therefore, with $\omega_C = 10 \text{ rad s}^{-1}$ ($\approx 95 \text{ rpm}$), the force ratio ($\bar{V}/2$) becomes 20. However, if ω_C increases up to 200 rad s^{-1} ($\approx 1,910 \text{ rpm}$), the force ratio becomes 1 so that the Coriolis force cannot be neglected with the above given characteristic values.

It should be mentioned that, in the previous works (Duffy et al. 1999; Madou et al. 2001) which were utilizing the centrifugal force, the ranges of the hydraulic radius and the rotational speed were from 10 to 170 μm

and from 10 to 118 rad s^{-1} , respectively. In these ranges of rotational speed and microchannel geometry, the Coriolis force could be negligible.

References

- Auroux P-A, Iossifidis D, Reyes DR, Manz A (2002) Micro total analysis systems. 2. Analytical standard operations and applications. *Anal Chem* 74:2637–2652
- Brenner T, Glatzel T, Zengerle R, Duce J (2003) A flow switch based on Coriolis force. In: *Proceedings of micro total analysis systems 2003*, 5–9 October 2003, Squaw Valley, CA, USA
- Duffy DC, Gillis HL, Lin J, Sheppard NF Jr, Kellogg GJ (1999) Microfabricated centrifugal microfluidic systems: characterization and multiple enzymatic assays. *Anal Chem* 71:4669–4678
- Effenhauser CS, Bruin GJM, Paulus A (1997) Integrated chip-based capillary electrophoresis. *Electrophoresis* 18:2203–2213
- Gyrolab™ microlaboratory—<http://www.gyros.com>
- Herr AE, Molho JI, Santiago JG, Mungall MG, Kenny TW, Garguilo MG (2000) Electroosmotic capillary flow with non-uniform zeta potential. *Anal Chem* 72:1053–1057
- Kim DS, Lee K-C, Kwon TH, Lee SS (2002) Micro-channel filling flow considering surface tension effect. *J Micromech Microeng* 12:236–246
- Koo J, Kleinstreuer C (2003) Liquid flow in microchannels: experimental observations and computational analyses of microfluidics effects. *J Micromech Microeng* 13:568–579
- Kovacs GTA (1998) *Micromachined transducers sourcebook*. WCB/McGraw-Hill, Boston
- Madou MJ, Lee LJ, Daunert S, Lai S, Shih C-H (2001) Design and fabrication of CD-like microfluidic platforms for diagnostics: microfluidic functions. *Biomed Microdevices* 3:245–254
- Manz A, Grabber N, Widmer HM (1990) Miniaturized total chemical analysis systems: a novel concept for chemical sensing. *Sens Actuators B* 1:244–248
- Probstein RF (1994) *Physicochemical hydrodynamics*. Wiley, New York
- Puntambekar A, Murugesan S, Trichur R, Cho HJ, Kim S, Choi J-W, Beaucage G, Ahn CH (2002) Effect of surface modification on thermoplastic fusion bonding for 3-D microfluidics, In: *Proceedings of micro total analysis systems 2002*, 3–7 November 2002, Nara, Japan
- Reyes DR, Iossifidis D, Auroux P-A, Manz A (2002) Micro total analysis systems 1. Introduction, theory, and technology. *Anal Chem* 74:2623–2636
- Ross D, Johnson TJ, Locascio LE (2001) Imaging of electroosmotic flow in plastic microchannels. *Anal Chem* 73:2509–2515
- Sanders GHW, Manz A (2000) Chip-based microsystems for genomic and proteomic analysis. *Trends Anal Chem* 19:364–378
- Tseng F-G, Yang I-D, Lin K-H, Ma K-T, Lu M-C, Tseng Y-T, Chieng C-C (2002) Fluid filling into micro-fabricated reservoirs. *Sens Actuators A* 97–98:131–138
- Xuan X, Li D (2004) Analysis of electrokinetic flow in microfluidic networks. *J Micromech Microeng* 14:290–298